Materials Horizons

ROYAL SOCIETY OF CHEMISTRY

COMMUNICATION

View Article Online
View Journal

Check for updates

Cite this: DOI: 10.1039/d5mh02107c

Received 5th November 2025,
Accepted 29th January 2026

DOI: 10.1039/d5mh02107c

rsc.li/materials-horizons

Uncovering a third function of the transistor beyond switching and amplification: coupled photo-responsive oscillators for in-sensor computing

Seong-Yun Yun,[a] Joon-Kyu Han[b] and Yang-Kyu Choi *[a]

To enable in-sensor computing that emulates the biological brain's ability to process visual information with minimal energy consumption, we demonstrated brain-inspired coupled twin photo-responsive oscillators (CT-PROs) that integrate sensing and signal processing within a single device. The CT-PROs utilize a single-transistor latch (STL) phenomenon to generate iterative oscillations modulated by incident light. Each PRO, structurally identical to a metal–oxide-semiconductor field-effect transistor (MOSFET), is capable of sensing optical stimuli and producing corresponding oscillatory outputs governed by the STL mechanism. Notably, the PRO obviates the need for an external photodetector because it inherently operates as both an oscillator and a photodetector, functioning as a Janus-like device. The oscillation characteristics vary with input light intensity and wavelength, enabling detection of both parameters by observing whether synchronization or desynchronization occurs between the CT-PROs under different illumination conditions. The CT-PROs can be used for a coupled oscillator network (CON) with in-sensor computing capabilities. As an application of the PRO-based CON, edge detection was conducted. Then, edge maps generated by the proposed CON were used to aid in classification. These results highlight the potential of PRO-based CONs for in-sensor vision systems.

New concepts

This work introduces a novel concept by redefining the traditional transistor's role beyond switching and amplification to function as a photo-responsive oscillator (PRO). Leveraging the single-transistor latch, the PRO generates oscillatory signals modulated by incident light intensity and wavelength. This dual-function device integrates sensing and signal processing within a single unit, eliminating the need for separate photodetectors and oscillators. Coupled twin PROs form a network capable of synchronized oscillations that process optical information for in-sensor computing. This enables efficient edge detection and image classification, with significant potential in low-energy vision systems. The PRO's compatibility with CMOS fabrication processes underscores its practicality for large-scale integration. Importantly, the concept represents a shift from traditional digital and static signal processing to dynamic, wave-based computation using coupled oscillators. Such a paradigm enhances noise robustness, energy efficiency, and scalability, which align with emerging neuromorphic and brain-inspired computing trends. This new framework fundamentally redefines sensor and processor integration, offering a promising direction for next-generation sensory and artificial intelligence systems.

Introduction

In situations where human lives are at risk or tasks are too complex for humans to perform, it has become essential to develop devices or robots capable of assisting or replacing human functions. Achieving such goals requires emulating the five human sensory modalities, which play a fundamental role in how we perceive and interact with the world. To date, extensive research efforts have focused on replicating human sensory capabilities, with particular emphasis on the visual system.[1] Among the senses, vision stands out as the most dominant modality, shaping our daily experiences and serving as the primary channel through which we engage with our environment. This dominance is reflected in the complexity of visual neural processing, which involves a significantly larger portion of the brain than other sensory systems. Notably, visual information processing consumes more energy than other sensory modalities, and this has made it a central focus in strategies aimed at reducing overall energy consumption.[2] In addition, vision is increasingly prioritized because of its critical role in managing the large volumes of information required for tasks such as pattern recognition, object detection, and image analysis.[3–6]

However, conventional vision systems based on the von Neumann architecture, which are structurally integrated with external photodetectors, are fundamentally limited by the inherent separation of photo-sensing, computation, and memory

---

[a] School of Electrical Engineering, Korea Advanced Institute of Science and Technology (KAIST), 291 Daehak-ro, Yuseong-gu, Daejeon 34141, Republic of Korea. E-mail: ykchoi@ee.kaist.ac.kr
[b] Department of Materials Science and Engineering and Inter-University Semiconductor Research Center, College of Engineering, Seoul National University, Gwanak-ro 1, Gwanak-gu, Seoul, 08826, South Korea

units.[7–10] This separation leads to significant energy consumption and latency resulting from frequent data transfers, which poses substantial challenges for applications that require real-time operation and low energy consumption, particularly when deployed in mobile devices, edge devices, and Internet of Things (IoT) environments. In-sensor computing provides an innovative approach to overcome these bottlenecks by enabling sensors to perform both signal acquisition and data pre-processing within a single unit. By integrating computation directly into the photodetector, in-sensor computing reduces redundant data transfers, increases computational speed, and enhances energy efficiency.[11,12]

Various forms of brain-inspired networks have been proposed as alternatives to the von Neumann architecture. Inspired by the synchronized oscillatory behaviour of biological neurons rather than discrete spikes in the brain, networks composed of coupled oscillators, known as coupled oscillator networks (CONs), offer smoother signal representation and simpler dynamics.[13–17] They are well suited for low-energy and real-time sensory systems given their inherently high energy efficiency, parallelism, and compatibility with analogue hardware.[18,19] Since CONs process information through phase relationships rather than complex arithmetic operations, unlike conventional networks that rely on deterministic functions, they are additionally more robust to noise. Therefore, if properly implemented, vision systems based on CONs can achieve simpler computation and lower energy consumption compared to conventional vision systems.

It is worth noting that signal processing based on wave-based oscillatory systems generally provides greater noise robustness, compared to traditional magnitude-centric linear approaches. This increased robustness is attributed to the inherent wave nature, where information is represented not only by amplitude but also by phase and frequency, enabling the system to selectively filter signals and utilize resonance effects to amplify relevant components while overcoming inevitable noise. Additionally, nonlinear interactions in coupled oscillators help them synchronize their phases collectively, making the system more resistant to disturbances. Wave-based systems can also encode information across both space and time, which helps protect against the effects of noise or damage in specific areas.

In this work, we propose coupled twin photo-responsive oscillators (CT-PROs) as a core element for a CON with in-sensor computing capabilities. The overall research concept is illustrated in Fig. 1a. The proposed PRO is equivalent to a metal–oxide-semiconductor field-effect transistor (MOSFET) and can thus be fabricated using mature complementary metal–oxide-semiconductor (CMOS) technologies developed over the past six

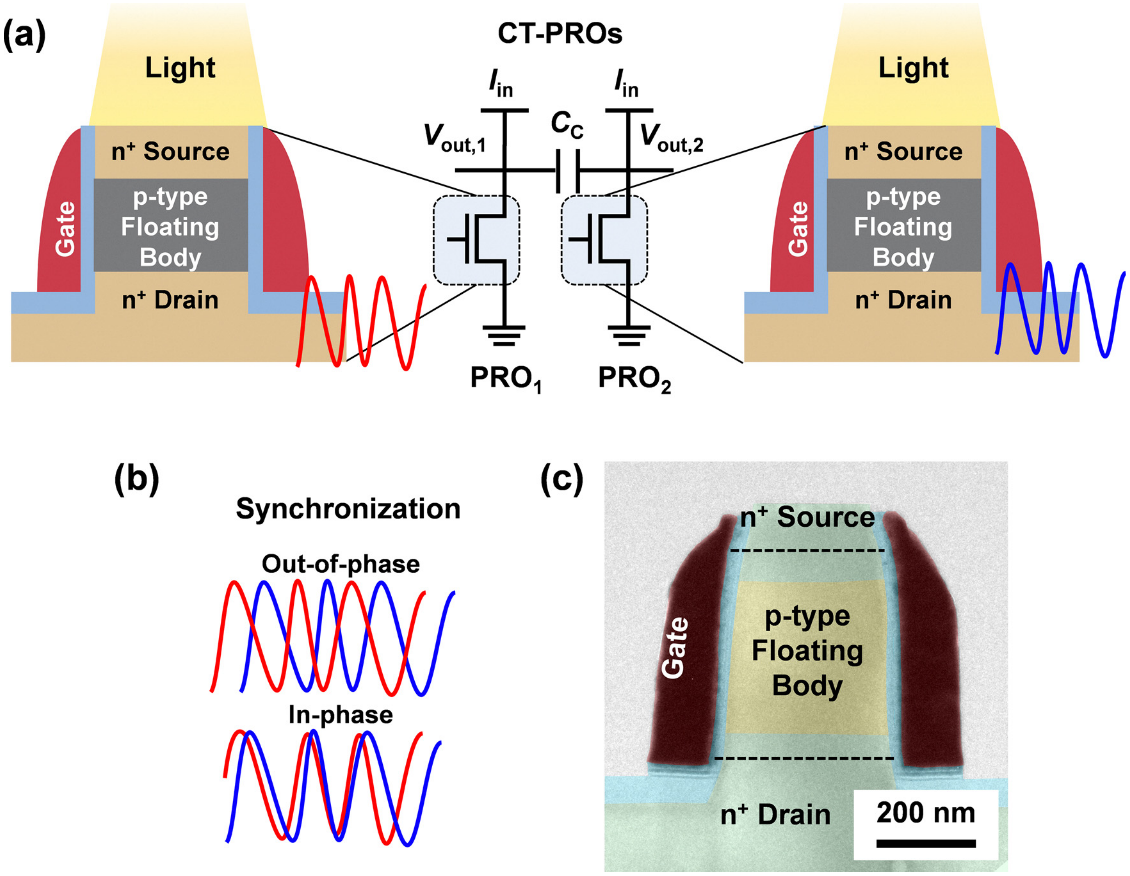

Fig. 1 Coupled twin photo-responsive oscillators (CT-PROs) for in-sensor computing. (a) Schematic illustration of the CT-PROs. Twin PROs (PRO_1 and PRO_2) are coupled through a coupled capacitor (C_C). (b) Schematic illustration of the two types of synchronization behaviour in CT-PROs: out-of-phase and in-phase synchronization. (c) Cross-sectional transmission electron microscopy (TEM) image of a single PRO. The n$^+$ source receives the illuminated light.

decades. This MOSFET comprises a source (S), a drain (D), a gate (G), and a floating body (FB). Traditionally, the body has been conceptualized as a resistive element, exhibiting high resistance in the off-state (R_{off}) and low resistance in the on-state (R_{on}). This conventional interpretation forms the basis for the term 'transistor', a combination of 'transfer' and 'resistor'. Within this framework, the transistor maintains a stable low current in the off-state and a high current in the on-state, independent of time. However, the present study offers a reinterpretation of the transistor's functional role by treating the FB not as a resistive but as a capacitive component. We experimentally demonstrate that a transistor incorporating an FB can function as an oscillator. The FB exhibits capacitive behaviour, undergoing continuous cycles of charging and discharging when a constant current is supplied to D. This process yields an oscillatory output, marking a functional transformation wherein the transistor operates not as a traditional electronic switch but as an active oscillator.

The MOSFET used in this work has a vertical pillar structure with the S/D positioned at the top and bottom of the pillar-shaped FB, respectively. The p-type single-crystalline silicon (Si) channel within the vertical pillar is physically isolated by a circular-shaped gate oxide and an n^+ *in situ* doped polycrystalline-silicon (poly-Si) gate, forming a gate-all-around (GAA) structure surrounding the channel. The channel (p-type Si) shares the same body region with the n^+ S and n^+ D, forming a FB due to the absence of an external electrical contact to the body. Since this FB can directly respond to external light stimuli for various light intensities (I_{L}) and wavelengths (λ), the PRO can function as a photodetector and a conventional transistor. Additionally, because the FB facilitates iterative oscillations through the single-transistor latch (STL) phenomenon, the PRO can also serve as the smallest unit of oscillatory processing.[20–22] Consequently, the PRO is capable of performing both sensing and processing functions for in-sensor computing. A building block of the CT-PROs consists of two photo-responsive oscillators (PRO_1 and PRO_2) connected *via* a coupling capacitor (C_{C}). An array of such CT-PROs collectively constitutes the coupled oscillator network (CON).

When the PRO is exposed to visible light, photogenerated electron–hole pairs (EHPs) accumulate in the FB, modulating the oscillation characteristics. After capacitively coupling the twin PROs, their synchronization behaviours were investigated by varying the I_{L} and λ of the illuminating light (Fig. 1b). As an application, edge detection was demonstrated based on measured synchronization behaviours. Furthermore, to evaluate the effectiveness of edge extraction across diverse images and its potential to enhance image recognition, software-based simulations employing convolutional neural networks (CNNs) were conducted.

Experimental

Fabrication of the PROs

The PROs were fabricated on a p-type silicon wafer. The fabrication details of the PROs are provided in Fig. S1 of the SI.

Electrical measurement

The electrical properties of the single PRO and the CT-PROs were measured using a semiconductor parameter analyser (B1500A, Keysight). The voltage source current measurement (VSCM) mode, which applies a voltage input and measures the resulting current output, was used to analyse output characteristics (drain current *vs.* drain voltage; I_{D}–V_{D}) with the STL. The current source voltage measurement (CSVM) mode, which applies a current input and measures the oscillating voltage output, was employed to characterize the oscillation behaviours. The switching speed of the PRO was measured by using a waveform generator fast measurement unit (WGFMU). The AC signal of a sine-wave was applied using an AC source (6221, Keithley).

Light illumination and analysis

For white light illumination, an LED light source (SOL 3.0, Fiber Optic Korea) was used. Red-, green-, and blue-coloured cellophane papers were utilized as colour filters to control the wavelength of the illuminating light. The light intensity was measured by using a power meter (PM100D, Thorlabs) and a photodiode power sensor (S120C, Thorlabs).

Circuit simulation

Circuit simulations were performed using SPICE software (LTspice, Analog Devices). Oscillating behaviour of the PRO was modelled with a voltage-controlled threshold switch and a parallel capacitor.

Image processing. Image processing for edge detection was performed using the Image Processing Toolbox in MATLAB. The CIFAR-10 dataset and ISIC 2018 dataset were used to demonstrate two-stream CNNs using edge maps.

Results and discussion

Photo-responsive oscillator (PRO)

Fig. 1c shows a cross-sectional transmission electron microscopy (TEM) image of the single PRO. The diameter (D_{p}) and height (H_{p}) of the fabricated vertical pillar are 400 nm and 700 nm, respectively. The fabrication procedure is illustrated in Fig. S1. This vertically structured MOSFET offers key advantages for large-scale implementation of the photo-responsive CONs. Its GAA configuration enhances scalability by effectively suppressing short-channel effects, while the vertical alignment of S, D, FB, and G enables higher integration density compared to conventional lateral configurations. Furthermore, the exposed S region improves photosensitivity by efficiently capturing incident light, making this architecture particularly well-suited for compact in-sensor vision systems.[23,24]

As a Janus-like device, the PRO functions in two distinct operating modes. The first mode, corresponding to conventional transistor operation, involves a voltage input (V_{in}) and current output (I_{out}); in this mode, a stationary drain current (I_{D}) without time dependence flows from D when the gate voltage (V_{G}) exceeds the threshold voltage (V_{T}). The second mode, functioning as an oscillator, is characterized by a current input (I_{in}) and a voltage output (V_{out}); here, an oscillating drain voltage (V_{D}) is generated at the D when V_{G} is below V_{T}.

When a positive V_{D} is applied along with a negative V_{G}, the PRO with an n-channel initially remains in a high-resistance state (HRS), with a small number of electrons overcoming the potential barrier between S and FB ($V_{\text{bi,S\_FB}}$). When V_{D} increases, EHPs are generated by impact ionization (II) near the junction between the FB and D. The generated holes accumulate in the FB, while the electrons move toward D. These accumulated holes reduce $V_{\text{bi,S\_FB}}$, enabling more electrons to flow from S to D, thereby amplifying the II through a positive feedback loop. This positive feedback loop induces a STL phenomenon, characterized by an abrupt transition from the HRS to a low-resistance state (LRS). When V_{D} reaches the latch-up voltage (V_{LU}), I_{D} increases suddenly by more than six orders of magnitude.

When a constant I_{in}, as a direct current (DC) input signal, is supplied to the D, the PRO initially in the HRS begins to integrate positive charges in a parasitic capacitor (C_{par}), which is parallelly connected at the D. This is a charging process. Here, C_{par} comprises the device capacitances and external capacitances. The former includes the capacitance of the large-sized probing pad, as well as the capacitances associated with G, S, D, and FB. The latter includes the capacitance of the measurement equipment and the cable capacitance used to connect the PRO to the measurement setup. This charging process causes V_{out} to increase until it reaches the top voltage (V_{top}), equivalent to the aforementioned V_{LU}. When V_{out} reaches V_{top}, the HRS switches to the LRS *via* the STL. Consequently, the integrated positive charges are abruptly discharged from C_{par}, resulting in a sudden drop in V_{out} to the bottom voltage (V_{bottom}). This is a discharging process. The voltage difference between V_{top} and V_{bottom} is defined as the peak-to-peak voltage (V_{pp}), *i.e.*, $V_{\text{top}} - V_{\text{bottom}}$. As long as I_{in} is forced, repetitive charging and discharging processes generate wedge-shaped oscillatory waveforms between V_{top} and V_{bottom} without requiring complex circuits.

Fig. S2 illustrates a detailed mechanism of the oscillation with energy band diagrams at each step. It is essential to investigate the oscillation characteristics of the PRO for various I_{in}, C_{par}, and D_{p} values. Fig. S3 shows its measured oscillation frequency (f) and energy consumption per oscillation (E/osc) for different I_{in} C_{par}, and D_{p} values. The f of the PRO can be simply modelled using the following equation:

$$f = \frac{I_{\text{in}}}{C_{\text{par}}\left(V_{\text{top}} - V_{\text{bottom}}\right)} = \frac{I_{\text{in}}}{C_{\text{par}}V_{\text{pp}}}$$

Both increasing I_{in} and the reduction of C_{par} increase f due to a higher speed of charge integration. As C_{par} decreases, f tends to increase, while E/osc tends to decrease. This result suggests that computing speed and energy efficiency can be further improved when C_{par} approaches the intrinsic capacitance of the PRO, by eliminating the extrinsic capacitance introduced by the measurement setup. As shown in Fig. S4, the measured switching speeds of the PRO from the HRS to the LRS and *vice versa* were 50 ns and 60 ns, respectively. Therefore, the maximum f of the PRO is expected to be 9.1 MHz, which is the reciprocal of the total switching delay. In addition, the oscillation characteristics also depend on D_{p}, which directly affects the effective channel width of the PRO. As D_{p} increases, the larger FB volume provides a higher effective capacity for hole storage, leading to an increased f and reduced E/osc.

As degradation of the oscillation characteristics can adversely affect system performance, it is worth evaluating the endurance of the PRO. Oscillating operations were continuously performed for 5×10^5 cycles. Fig. S5a–c show that there was no noticeable degradation in V_{top} and f during long-term operation. Also, Fig. S5d compares the transfer characteristics ($I_{\text{D}} - V_{\text{G}}$) of the PRO before and after this endurance test, showing a negligible change in threshold voltage, subthreshold swing, and gate current. These results confirm that the performance of the PRO can be maintained under repetitive operation.

Photo-responsive characteristics of the PRO

When the I_{L} and/or λ are varied, the f of the PRO responds accordingly. These characteristics enable the PRO to perform in-sensor computing by detecting two distinct types of optical information. When I_{in} is applied to the PRO, the STL is electrically triggered, leading to the generation of EHPs through II. Among the EHPs, the electrically generated holes accumulate within the FB, reducing $V_{\text{bi,S\_FB}}$. As more electrons are injected into the FB, the II process is further accelerated, amplifying the generation of EHPs. These sequential processes constitute a positive feedback loop.

When the electrically activated PRO, which was biased by the applied I_{in}, is exposed to visible light, additional EHPs are generated by incident photons, as illustrated in Fig. 2a. Although the FB is partially shielded by the S electrode, visible light can still effectively influence the FB region because the interlayer dielectric (ILD) is transparent and the thickness of the S region is sufficiently small compared with the penetration depth of visible light in silicon, particularly at longer λ. Consequently, photocarriers generated in the S region can diffuse and drift into the FB. The optically generated holes additionally reduce $V_{\text{bi,S\_FB}}$, resulting in a decrease in V_{LU} with increasing I_{L}, as shown in Fig. 2b. In this proof-of-concept demonstration, white light was used as the illumination source with the fixed λ. As I_{L} increases, more EHPs are optically generated, further lowering $V_{\text{bi,S\_FB}}$. This, in turn, leads to reductions in both V_{top} and V_{pp}, while simultaneously increasing f, as shown in Fig. 2c–e. Through this mechanism, the PRO functions dually as a photodetector and an oscillator.

The electrical characteristics of the PRO also depend on λ. Fig. 3a shows the energy band diagrams with different λ values of the illuminated light with the fixed I_{L}. The PRO was exposed to light in the visible spectrum (red, green, and blue) using a white light source and a colour filter. As λ increases, the penetration depth of photons into silicon also increases.[25,26] In the PRO, the key factor governing the λ dependence is the spatial distribution of photogenerated EHPs, particularly the distance between their peak generation point and the junction boundary between the n^+ S and the p-type FB. Shorter λ is strongly absorbed near the n^+ S, where carrier recombination is

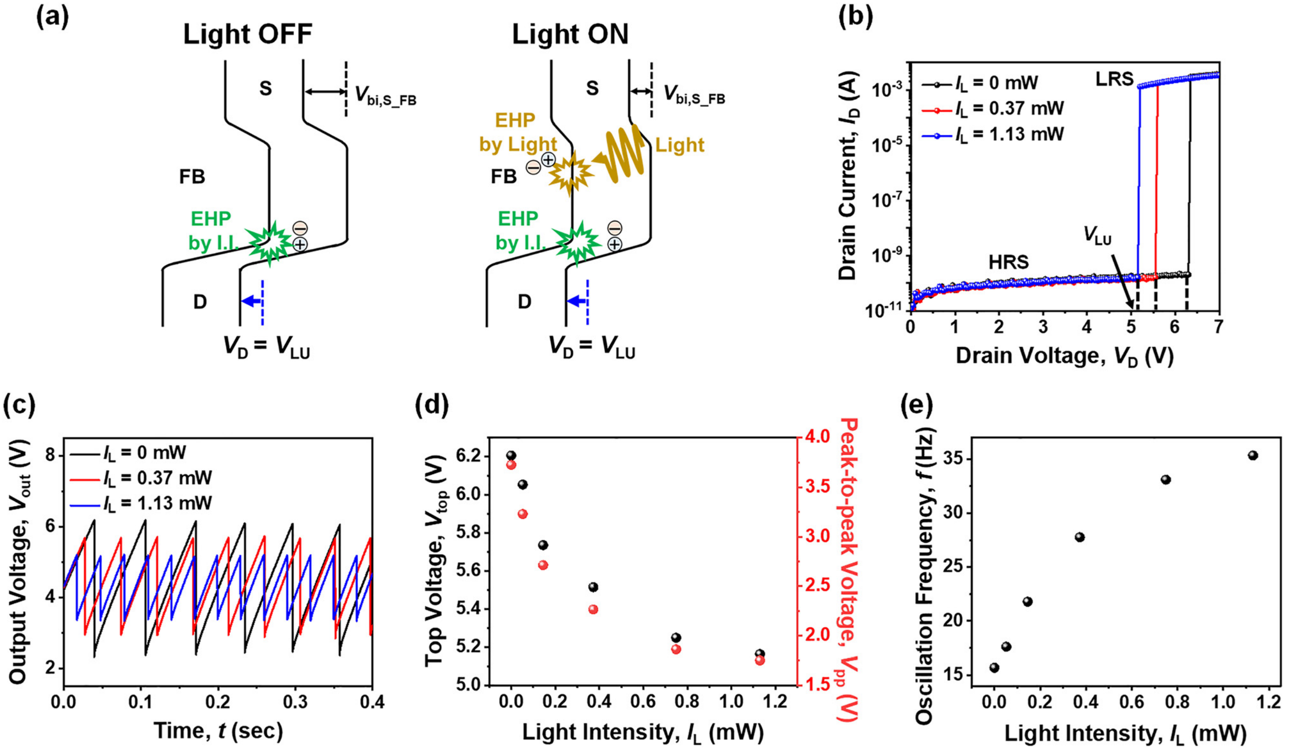

Fig. 2 Light intensity-dependent electrical properties of the PRO. (a) Energy band diagrams without light illumination (left) and with light illumination (right). (b) Measured output characteristics (I_D–V_D) for different light intensities (I_L). The single transistor latch (STL) phenomenon is observed. Latch-up voltage (V_{LU}) depends on I_L. (c) Measured oscillation characteristics (V_{out}–t) for different I_L values. (d) Extracted top voltage (V_{top}) and peak-to-peak voltage (V_{pp}) as a function of I_L. (e) Extracted oscillation frequency (f) as a function of I_L. As I_L increases, f increases due to the reduced V_{pp}.

significant and their influence on the FB is limited. In contrast, longer λ, such as red light in this work, penetrates deeper into the p-type FB region, thereby more effectively modulating the hole population in the FB. Therefore, the values of V_{top}, V_{pp}, and f in the oscillation, as well as V_{LU} in the STL, are influenced by λ (Fig. 3b–e). In this way, the PRO simultaneously detects light and encodes light information into oscillations.

Characteristics of the coupled twin PROs

Following the analysis of the PRO's electrical and optical characteristics, preliminary investigations into the synchronization behaviour of the CT-PROs, as a core element of a CON, were conducted in the absence of light. Fig. S6a shows the circuit diagram of the CT-PROs, where the output voltages ($V_{out,1}$ and $V_{out,2}$) are coupled *via* the coupling capacitance (C_C). Their synchronization behaviours change according to C_C (Fig. S6b).

Fig. S6c presents the measured $V_{out,1}$ and $V_{out,2}$, while Fig. S6d shows the averaged XOR (AV_{XOR}) value, which is adopted to quantify synchronization behaviours. The AV_{XOR} measures the degree of similarity between waveforms, and this method has been reliably used to assess synchronization.[27–29] To calculate AV_{XOR}, $V_{out,1}$ and $V_{out,2}$ are converted into binary values (*i.e.*, 0 or 1) using a thresholding process, after which the XOR operation is performed on them. The result of this operation is then averaged over time. When C_C is less than 20 pF, $V_{out,1}$ and $V_{out,2}$ fluctuate independently. The coupling is too weak to enable effective charge exchange between the twin PROs, resulting in a lack of correlation. Consequently, AV_{XOR} fluctuates randomly over time and converges to 0.5, indicating no synchronization.

In contrast, when C_C exceeds 5.6 nF, the twin PROs synchronize with a phase difference ($\Delta\phi$) of 0°, corresponding to in-phase synchronization and an AV_{XOR} value approaching 0. At intermediate C_C values between these two extremes, out-of-phase synchronization with a $\Delta\phi$ of 180° (π) is observed. In this range, AV_{XOR} gradually decreases with increasing C_C, indicating a transition from uncorrelated to correlated behaviour characterized by in-phase synchronization. It is important to note that under practical operating conditions, a dedicated readout circuit can be used for signal input and output, avoiding the need for external instruments such as a parameter analyser. This configuration helps eliminate the influence of external capacitance, whose magnitude is comparable to that of C_C, and therefore leads to a significant reduction in the total capacitance.

To examine the robustness of spontaneous synchronization against noise in the CT-PROs, a controlled noisy input was intentionally applied to one of the PROs, as shown in Fig. S7a. A constant direct current (I_{DC}) was supplied to PRO_1, while a time-varying alternating current (I_{AC}) superimposed on the same I_{DC} was applied to PRO_2. Fig. S7b presents $V_{out,1}$ and $V_{out,2}$ for various I_{AC} amplitudes. Out-of-phase synchronization was consistently observed regardless of the magnitude of I_{AC}. As shown in Fig. S7c and d, a comparison of the fast Fourier transform (FFT) spectra with and without I_{AC} injection indicates that the f of the CT-PROs was not significantly altered. To better emulate

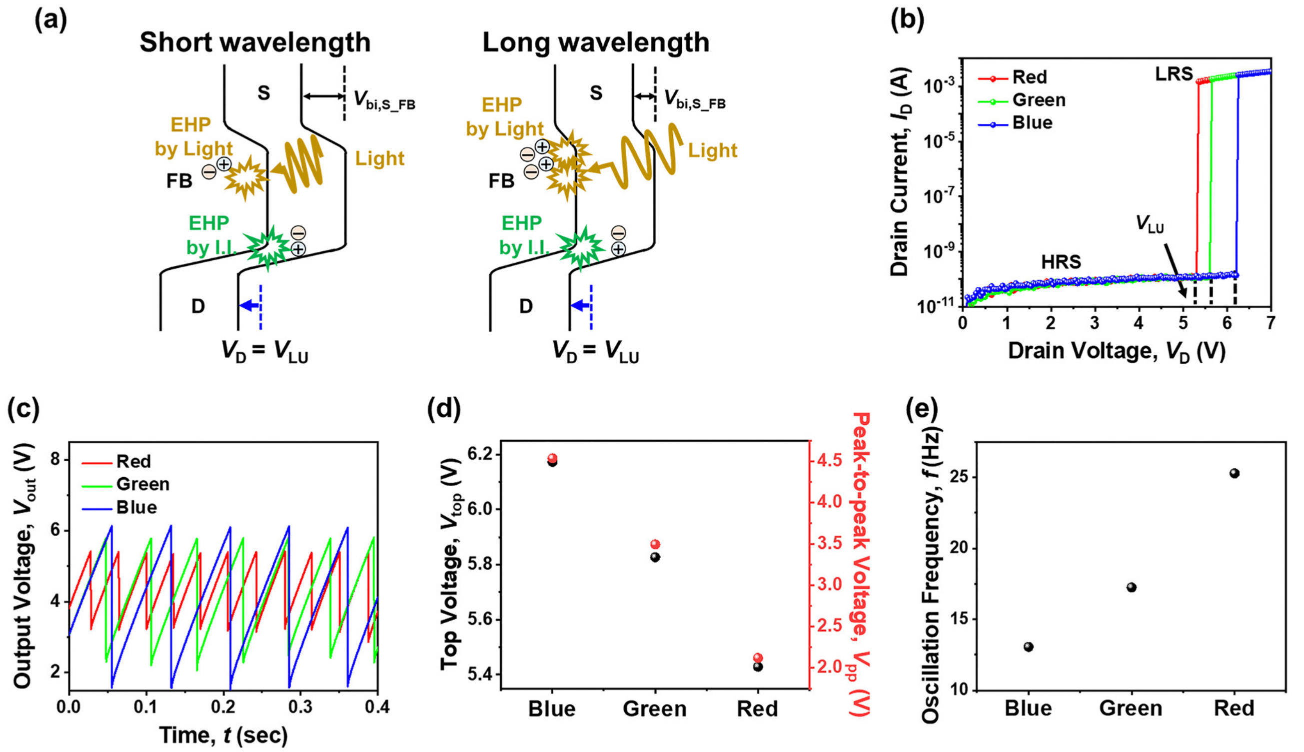

Fig. 3 Wavelength-dependent electrical properties of the PRO. (a) Energy band diagrams with short-wavelength light illumination (left) and long-wavelength light illumination (right). (b) Measured I_D–V_D for different wavelengths (λ). V_{LU} also depends on λ. (c) V_{out}–t for different λ values. (d) Extracted V_{top} and V_{pp} as a function of λ. (e) Extracted f as a function of λ. As λ increases, f increases due to the reduced V_{pp}.

real environments, semi-empirical simulations were conducted using the SPICE circuit simulator. As depicted in Fig. S8a, the PRO was modelled as a voltage-controlled threshold switch connected in parallel with a C_{par}. The simulated output, shown in Fig. S8b, closely matched the experimental results. In the simulation setup (Fig. S8c and d), a constant I_{DC} was supplied to PRO_1 as a reference, while an IAC with randomly fluctuating noise superimposed on the same I_{DC} was applied to PRO_2. As presented in Fig. S8e and f, the waveform and FFT spectra exhibited a minimal change despite the presence of noise. This high level of noise immunity demonstrates the suitability of CT-PROs for integration into noise-resilient CONs.

Next, the synchronization behaviours of the CT-PROs under the different combinations of light illumination were investigated. Two light sources were independently controlled to apply various I_L and λ values to the CT-PROs. In Fig. 4a–c, synchronization behaviours are investigated by adjusting only I_L of the white light incident on each PRO, with I_L levels categorized as low, middle, and high. In contrast, Fig. 4d–f explore synchronization behaviours while adjusting only λ of the light incident on each PRO, with λ classified as red, green, and blue.

Fig. 4a illustrates a circuit configuration where PRO_1 and PRO_2 are connected through a C_C of 200 pF and subjected to illumination with different I_L values. When low, middle, and high I_L levels are applied to PRO_1 and PRO_2, respectively, the maximum number of possible I_L combinations is nine, forming a 3-by-3 matrix. As shown in Fig. S9a, when CT-PROs receive light of the same I_L (*e.g.*, low, middle, or high), they oscillate with similar V_{pp} values in $V_{out,1}$ and $V_{out,2}$, readily exhibiting out-of-phase synchronization. For example, as shown in Fig. 4b, when CT-PROs are exposed to low I_L, strong coupling occurs, resulting in effective synchronization. In contrast, when one PRO is illuminated with low I_L and the other with high I_L, the coupling weakens, leading to less coherent synchronization. This variation in synchronization behaviour is also reflected in AV_{XOR} values, as shown in Fig. 4c. A higher AV_{XOR} value indicates more coherent synchronization. The AV_{XOR} increases as the I_L levels of the CT-PROs become more similar, indicating that synchronization becomes more pronounced when the CT-PROs are illuminated with comparable I_L.

Similarly, synchronization behaviour also depends on the λ of the illuminating light. Fig. 4d presents another circuit diagram in which PRO_1 and PRO_2 are coupled through the same C_C of 200 pF and are exposed to light of various λ values. The twin PROs are independently illuminated with nine λ combinations, corresponding to a 3-by-3 matrix of red/green/blue light applied to PRO_1 and PRO_2, respectively. As shown in Fig. 4e, f, and S9b when the CT-PROs receive light with the same λ (*e.g.*, red, green, or blue), strong coupling facilitates coherent out-of-phase synchronization with higher AV_{XOR} values. However, when one PRO receives red light, while the other receives blue light, the coupling weakens, leading to deteriorated out-of-phase synchronization and lower AV_{XOR} values.

Unlike the previous cases, where only I_L or λ was varied, light information under diverse illumination conditions becomes more complex. Independently adjusting both I_L and λ for each

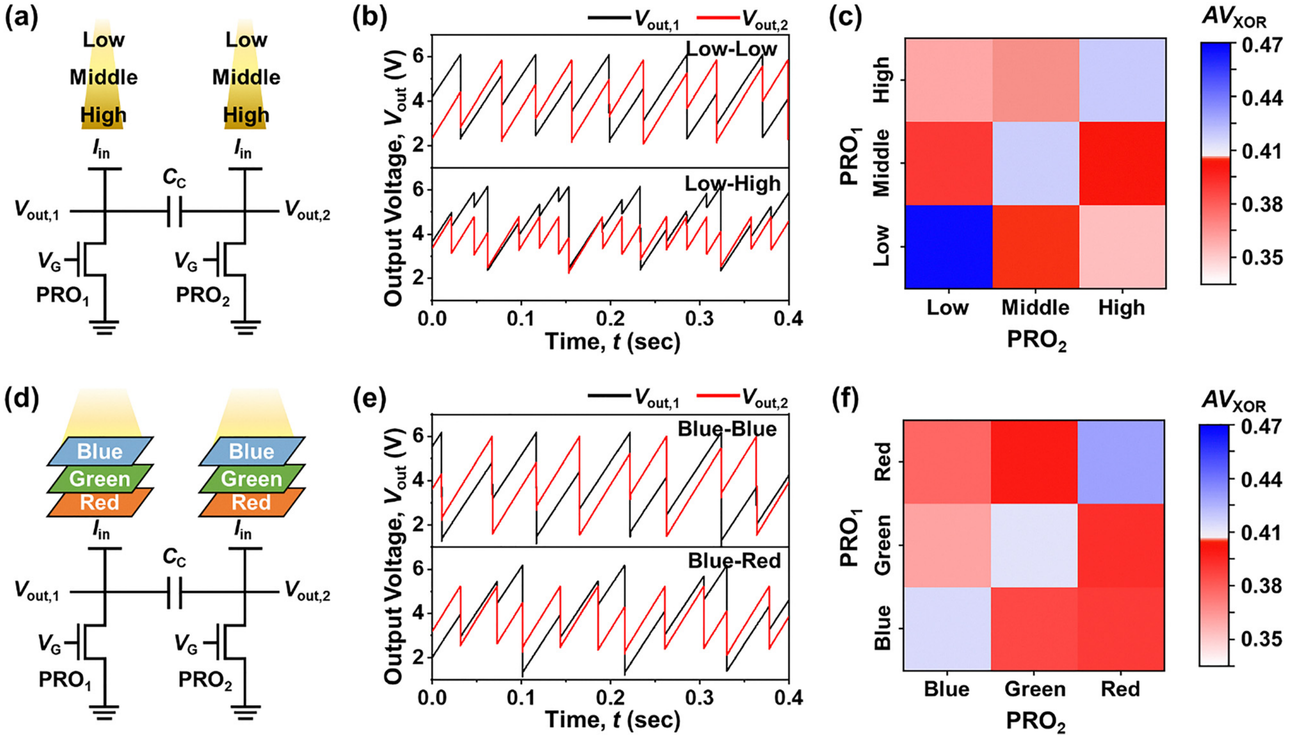

Fig. 4 Measured characteristics of the CT-PROs at various I_L and λ values, with one parameter fixed. (a) Circuit diagram of the CT-PROs independently illuminated by various I_L values, while λ is fixed. The output voltages ($V_{out,1}$ and $V_{out,2}$) are coupled *via* C_C. (b) Comparison of measured $V_{out,1}$ and $V_{out,2}$ under different I_L conditions for coherent and less coherent coupling. In the top plot, both PROs are illuminated with low I_L. In the bottom plot, one PRO is illuminated with low I_L, while the other is illuminated with high I_L. (c) Heatmap of the averaged XOR (AV_{XOR}) values from the CT-PROs over time for different I_L combinations. (d) Circuit diagram of the CT-PROs independently illuminated by various λ values, while I_L is fixed. (e) Comparison of measured $V_{out,1}$ and $V_{out,2}$ under different λ conditions for coherent and less coherent coupling. In the top plot, twin PROs are illuminated with blue light. In the bottom plot, one PRO is illuminated with blue light, while the other is illuminated with red light. (f) Heatmap of the AV_{XOR} values from the CT-PROs over time for different λ combinations.

oscillator results in 81 possible combinations, corresponding to a 9-by-9 matrix comprising I_L values of low/middle/high and λ values of red/green/blue, applied to PRO$_1$ and PRO$_2$, respectively. Fig. S10a presents the circuit diagram for 81 combinations, covering three values of I_L and three values of λ for the CT-PROs. As shown in Fig. S10b, the results indicate that similar conditions of I_L and λ for CT-PROs produce higher AV_{XOR} values. In contrast, mismatched conditions generally result in lower AV_{XOR} values.

Edge detection with the coupled twin PROs

Edge detection is a fundamental technique for distinguishing lines and edges within an image. It is used to identify boundaries where pixel values change abruptly, producing an edge map that highlights object contours.[30,31] A line refers to a region where adjacent pixels exhibit similar intensity values, while an edge corresponds to a region characterized by a significant intensity difference between neighbouring pixels. To demonstrate edge detection, CT-PROs were employed, with each PRO representing a single pixel based on experimentally obtained AV_{XOR} values. The AV_{XOR} value associated with each pixel pair was monitored to assess synchronization behaviour. High AV_{XOR} values, indicating coherent synchronization, were interpreted as lines, whereas low AV_{XOR} values, reflecting less coherent synchronization, signified edges.

The edge detection was performed under three scenarios: (1) when only I_L was considered, (2) when only λ was considered, and (3) when both I_L and λ were considered. Fig. S11 categorizes the three scenarios and provides procedural details. When only I_L was considered, an image was converted into a grayscale image. When only λ was considered, the image was converted into an image composed solely of red/green/blue pixels. In the combined scenario, both of them were used for edge detection, identifying edges where either I_L or λ of two neighbouring pixels differ.

Edge detection simulations were performed using MATLAB by scanning the image and observing the AV_{XOR} values between adjacent pixel pairs, as shown in Fig. 5. The scanning process involved both vertical and horizontal movements. Horizontal scanning involved sequential movements from left to right, while vertical scanning moved sequentially from top to bottom. As shown in Fig. S12, for vertical edge detection, the CT-PROs were placed vertically—one above the other—and an AV_{XOR} value from the top and bottom pixels was extracted using a monotone grayscale. Similarly, for lateral edge detection, the CT-PROs were placed side-by-side, and an AV_{XOR} value from left and right pixels was obtained in the same manner. As shown in Fig. S13, the scenario that considered both I_L and λ resulted in the highest number of detected edges, demonstrating that simultaneous scanning of both parameters enhances edge detection performance.

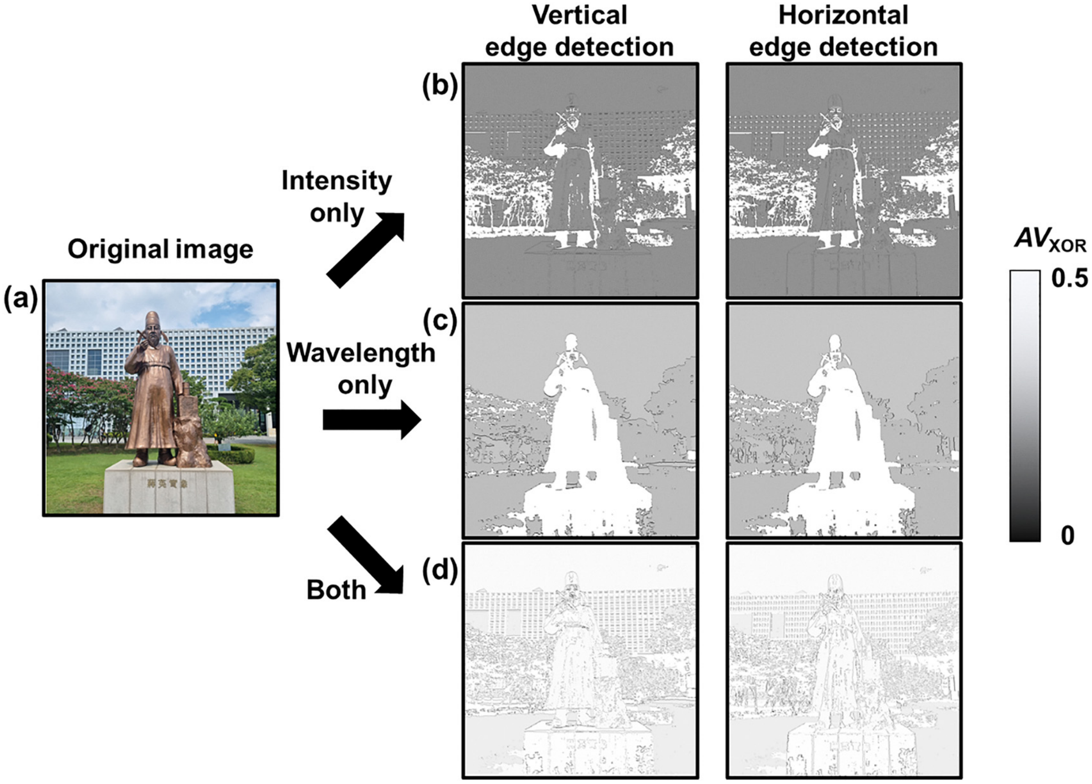

Fig. 5 Edge detection with the CT-PROs. (a) Original image for edge detection. (b) Vertical and horizontal edge detection based on I_L solely. (c) Vertical and horizontal edge detection based on λ solely. (d) Vertical and horizontal edge detection considering both I_L and λ, integrating both information to detect edges more effectively.

To investigate the benefits of integrating edge detection in classification tasks, we constructed two convolutional neural networks (CNNs): a conventional one-stream CNN using only original images and a two-stream CNN that integrates original images and edge maps. To assess the utility of edge information as a complementary feature in visual recognition, we used the Canadian Institute for Advanced Research (CIFAR)-10 dataset, which consists of 50 000 training and 10 000 test images (Table S1).[32]

Edge maps were generated in advance using the CON based on the CT-PROs, where a predefined threshold was applied to binarize the AV_{XOR} output (Fig. S14). The resulting edge maps were compared with those obtained using the Canny and Sobel edge detection algorithms.[33–35] Under the scenario considering both I_L and λ, the CT-PROs exhibited edge detection performance comparable to these conventional methods, while significantly reducing hardware resources and energy consumption by eliminating multiple kernel matrices.

Fig. 6a depicts the one-stream and two-stream CNN architectures. The two-stream CNN comprises two parallel pathways for original images and edge maps, each including convolutional layers, ReLU activation layers, and max pooling layers. An element-wise attention mechanism is applied prior to fusion, where attention weights derived from the edge stream modulate the original image features.[36] The fused features are then concatenated and passed through a dropout layer and a fully connected layer for final classification. For a fair comparison, the one-stream CNN shares the same convolutional structure and both models were trained under identical conditions. Detailed information of the network is provided in Table S2.

As shown in Fig. 6b, the two-stream CNN that incorporated edge maps achieved higher classification accuracy than the one-stream CNN. In addition, the corresponding confusion matrices in Fig. 6c and S15 showed enhanced classification performance. This classification performance can be further improved through techniques such as employing pretrained networks, optimizing data structures, and applying learning rate scheduling. To further validate generalizability, the two-stream CNN was evaluated on the International Skin Imaging Collaboration (ISIC) 2018 skin lesion dataset (Fig. S16), where it consistently outperformed the one-stream CNN.[37]

The results from these semi-empirical simulations demonstrate that edge maps function as valuable structural priors, allowing the network to effectively capture boundary and contour information that cannot be readily inferred from the original images alone. By explicitly integrating edge representations, the model is better equipped to learn both visual and structural features in a complementary manner. Furthermore, the inclusion of an attention mechanism amplifies the contribution of edge features. Collectively, the integration of edge maps significantly enhances classification performance, particularly in categories where structural information is critical.

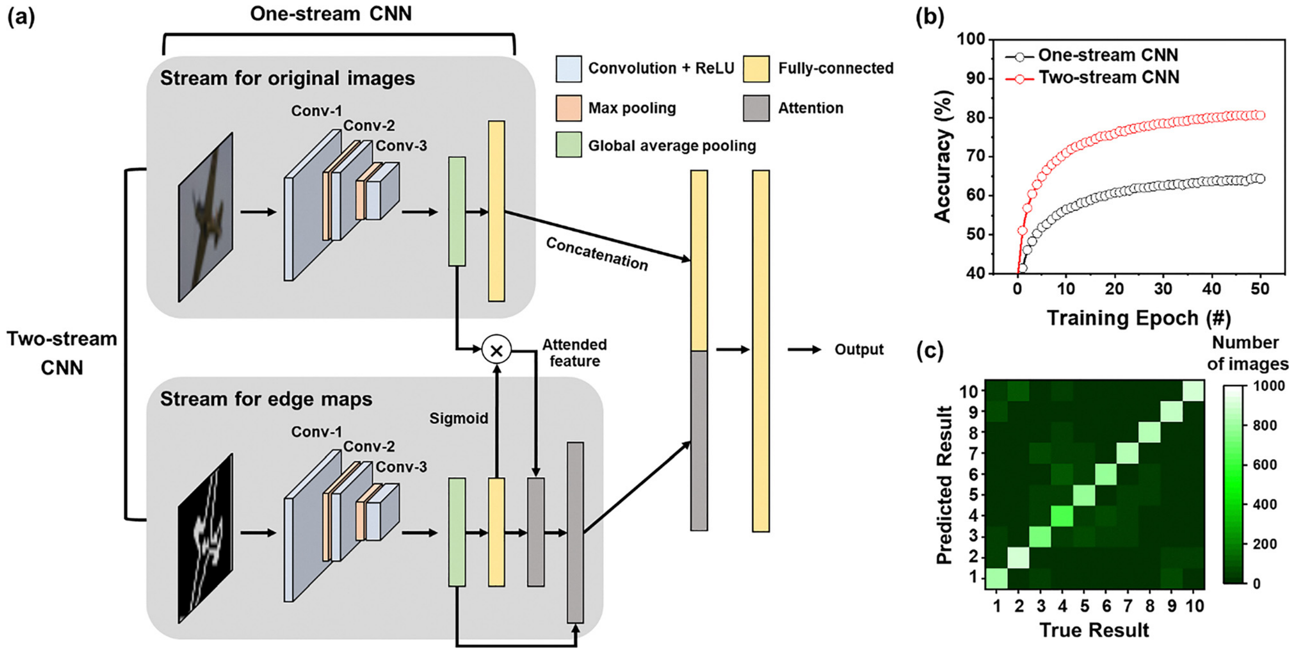

Fig. 6 Comparison of classification accuracy between the conventional one-stream convolutional neural network (CNN) and the two-stream CNN assisted by edge maps generated using the CT-PROs. (a) Architectures of CNNs for two types: conventional one-stream CNN (upper gray box) and two-stream CNN (upper and lower gray boxes). In the case of the two-stream CNN, edge maps generated through edge detection using the CT-PROs were utilized as supplementary input. (b) Comparison of classification accuracy between the conventional one-stream CNN and the two-stream CNN over the number of epochs. The two-stream CNN outperforms the conventional one-stream CNN. (c) Confusion matrix of classification results from the two-stream CNN.

Conclusions

This work aims to identify a third function of the MOSFET, beyond switching and amplification, by re-envisioning it as an oscillator. It further demonstrates the feasibility of integrating sensing and computing through coupled twin photo-responsive oscillators (CT-PROs), which, owing to their wave-based characteristics, facilitate the development of energy-efficient and noise-resilient vision systems. Although the PRO is based on a conventional MOSFET structure, it operates as both a photodetector and an oscillator, similar to a Janus-like device. Its distinguishing feature lies in the utilization of wave signals rather than static signals, *i.e.*, it produces oscillating output voltages in response to an input current, in contrast to the conventional behaviour of a MOSFET, which generates a constant output current from a steady input voltage. By exploiting the light-modulated oscillation characteristics of the PRO, in-sensor computing capabilities were achieved. The PRO detects both light intensity and wavelength, enabling sensory information processing. The degree of synchronization in the CT-PROs varies with light illumination conditions. The successful implementation of edge detection using the CT-PROs *via* semi-empirical simulations highlights their potential for real-time image processing applications. A benchmark table comparing the proposed PRO with previously reported oscillators for visual recognition is provided in Table S3. The in-sensor computing implemented within an oscillatory framework offers a promising direction for next-generation sensory systems. This approach enables improved energy efficiency through wedge-shaped oscillation waveforms, enhanced scalability due to compatibility with CMOS technology, and increased noise immunity as a result of the intrinsic properties of wave-based signal processing. Moreover, the compatibility of CT-PROs with mature CMOS fabrications suggests their viability for large-scale integration, making them promising candidates for advanced vision-based artificial intelligence applications.

Author contributions

S.-Y. Yun and J.-K. Han conceived the research idea. S.-Y. Yun performed the measurement and the software simulation. S.-Y. Yun wrote the manuscript. Y.-K. Choi supervised the whole research and edited the manuscript.

Conflicts of interest

There are no conflicts to declare.

Data availability

The data supporting this article have been included as part of the manuscript and its supplementary information (SI). Supplementary information is available. See DOI: https://doi.org/10.1039/d5mh02107c.

Acknowledgements

This work was supported in part by the National Research Foundation of Korea under grants RS-2023-00260637, RS-2023-00217888, RS-2024-00333710, and RS-2025-04162969.

Notes and references

1 F. Hutmacher, *Front. Psychol.*, 2019, **10**, 481030.
2 M. Wong-Riley, *Eye Brain*, 2010, **99**, 99–116.
3 F. Zhou, Z. Zhou, J. Chen, T. H. Choy, J. Wang, N. Zhang, Z. Lin, S. Yu, J. Kang, H.-S. P. Wong and Y. Chai, *Nat. Nanotechnol.*, 2019, **14**, 776.
4 M. Javaid, A. Haleem, R. P. Singh, S. Rab and R. Suman, *Sens. Int.*, 2022, **3**, 100132.
5 C. Wan, P. Cai, M. Wang, Y. Qian, W. Huang and X. Chen, *Adv. Mater.*, 2020, **32**, 1902434.
6 G. J. Lee, C. Choi, D. Kim and Y. M. Song, *Adv. Funct. Mater.*, 2017, **28**, 1705202.
7 J. Woo Park and D. S. Jeon, *IDEC J. Integr. Circuits Syst.*, 2020, **6**, 17.
8 M. A. Zidan, J. P. Strachan and W. D. Lu, *Nat. Electron.*, 2018, **1**, 22.
9 C. D. Schuman, S. R. Kulkarni, M. Parsa, J. P. Mitchell, P. Date and B. Kay, *Nat. Comput. Sci.*, 2022, **2**, 205.
10 N. Talati, R. Ben-Hur, N. Wald, A. Haj-Ali, J. Reuben and S. Kvatinsky, *Applications of Emerging Memory Technology: Beyond Storage*, Springer Singapore, 2019.
11 J.-K. Han, S.-Y. Yun, S.-W. Lee, J.-M. Yu and Y.-K. Choi, *Adv. Funct. Mater.*, 2022, **32**, 2204102.
12 T. Wan, B. Shao, S. Ma, Y. Zhou, Q. Li and Y. Chai, *Adv. Mater.*, 2022, **35**, 2203830.
13 A. Parihar, N. Shukla, M. Jerry, S. Datta and A. Raychowdhury, *Sci. Rep.*, 2017, **7**, 911.
14 S.-Y. Yun, J.-K. Han and Y.-K. Choi, *Nano Lett.*, 2024, **24**, 2751.
15 S. Dutta, A. Khanna, A. S. Assoa, H. Paik, D. G. Schlom, Z. Toroczkai, A. Raychowdhury and S. Datta, *Nat. Electron.*, 2021, **4**, 502.
16 N. Mohseni, P. L. McMahon and T. Byrnes, *Nat. Rev. Phys.*, 2022, **4**, 363.
17 D. E. Nikonov, G. Csaba, W. Porod, T. Shibata, D. Voils, D. Hammerstrom, I. A. Young and G. I. Bourianoff, *IEEE J. Explor. Solid-State Comput. Devices Circuits*, 2015, **1**, 85.
18 G. Csaba and W. Porod, *Appl. Phys. Rev.*, 2020, **7**, 1.
19 C. Delacour, S. Carapezzi, G. Boschetto, M. Abernot, T. Gil, N. Azemard and A. Todri-Sanial, *Neuromorphol. Comput. Eng.*, 2023, **3**, 034004.
20 C.-D. Chen, M. Matloubian, R. Sundaresan, B.-Y. Mao, C. C. Wei and G. P. Pollack, *IEEE Electron Device Lett.*, 1988, **9**, 636.
21 S.-Y. Yun, J.-K. Han, S.-W. Lee, J.-M. Yu, S.-B. Jeon and Y.-K. Choi, *Nano Energy*, 2023, **109**, 108322.
22 J.-W. Jung, J.-K. Han, J.-M. Yu, M.-W. Lee, M.-S. Kim, G.-B. Lee, I.-W. Tcho, S.-Y. Yun and Y.-K. Choi, *IEEE Electron Device Lett.*, 2022, **43**, 1359.
23 J.-K. Han, S.-Y. Yun, J.-M. Yu, S.-B. Jeon and Y.-K. Choi, *ACS Appl. Mater. Interfaces*, 2023, **15**, 5449.
24 J.-K. Han, D.-M. Geum, M.-W. Lee, J.-M. Yu, S. K. Kim, S. Kim and Y.-K. Choi, *Nano Lett.*, 2020, **20**, 8781–8788.
25 J. Xue, Z. Zhu, X. Xu, Y. Gu, S. Wang, L. Xu, Y. Zou, J. Song, H. Zeng and Q. Chen, *Nano Lett.*, 2018, **18**, 7628.
26 Y. R. Sipauba Carvalho da Silva, R. Kuroda and S. Sugawa, *Sensors*, 2019, **19**, 2755.
27 N. Shukla, A. Parihar, M. Cotter, M. Barth, X. Li, N. Chandramoorthy, H. Paik, D. G. Schlom, V. Narayanan, A. Raychowdhury and S. Datta, 2014 IEEE International Electron Devices Meeting, 2014, 28.7.1.
28 H. Eslahi, T. J. Hamilton and S. Khandelwal, *IEEE J. Explor. Solid-State Comput. Devices Circuits*, 2020, **6**, 122.
29 S.-Y. Yun, Y.-S. Chung, J.-K. Han, S.-W. Lee and Y.-K. Choi, *IEEE Trans. Electron Devices*, 2025, **72**, 494.
30 A.-V. Diaconu and I. Sima, Proceedings of the International Conference on Electronics, Computers And Artificial Intelligence – ECAI-2013, 2013, vol. 1.
31 J. Canny, *IEEE Trans. Pattern Anal. Mach. Intell.*, 1986, **6**, 679.
32 A. Krizhevsky, Learning multiple layers of features from tiny images 2009, https://www.cs.toronto.edu/~kriz/cifar.html.
33 M. Abernot and A. Todri-Sanial, *Neuromorphol. Comput. Eng.*, 2023, **3**, 014006.
34 C. Delacour, S. Carapezzi, M. Abernot and A. Todri-Sanial, *IEEE Trans. Neural Network Learn. Syst.*, 2024, **35**, 10045.
35 M. Abernot, T. Gil and A. Todri-Sanial, Proc. Neuro-Inspired Comput. Elements Conf., 2022, pp. 13–21.
36 Z. Niu, G. Zhong and H. Yu, *Neurocomputing*, 2021, **452**, 48–62.
37 N. Codella, V. Rotemberg, P. Tschandl, M. E. Celebi, S. Dusza, D. Gutman, B. Helba, A. Kalloo, K. Liopyris, M. Marchetti, H. Kittler and A. Halpern, Skin lesion analysis toward melanoma detection 2018: a challenge hosted by the international skin imaging collaboration (isic) 2019, https://arxiv.org/abs/1902.03368.